The Astrophysical Journal, 784:130 (11pp), 2014 April 1 doi:10.1088/0004-637X/784/2/130
© 2014. The American Astronomical Society. All rights reserved. Printed in the U.S.A.

THE HEATING OF MID-INFRARED DUST IN THE NEARBY GALAXY M33: A TESTBED FOR TRACING GALAXY EVOLUTION

Marie D. Calapa[1], Daniela Calzetti[1], Bruce T. Draine[2], Médéric Boquien[3], Carsten Kramer[4], Manolis Xilouris[5], Simon Verley[6], Jonathan Braine[7], Monica Relaño[8], Paul van der Werf[9], Frank Israel[10], Israel Hermelo[11], and Marcus Albrecht[12]

[1] Department of Astronomy, University of Massachusetts, 710 North Pleasant Street, Amherst, MA 01003, USA; mcalapa@umass.edu, calzetti@astro.umass.edu
[2] Princeton University Observatory, Peyton Hall, Princeton, NJ 08544-1001, USA; draine@astro.princeton.edu
[3] Institute of Astronomy, University of Cambridge, Madingley Road, Cambridge, CB3 0HA, UK; mboquien@ast.cam.ac.uk
[4] Instituto de Radio Astronoma Milimétrica (IRAM), Avenida Divina Pastora 7, Local 20, E-18012 Granada, Spain; kramer@iram.es
[5] Institute for Astronomy, Astrophysics, Space Applications & Remote Sensing, National Observatory of Athens, P. Penteli, 15236 Athens, Greece; xilouris@astro.noa.gr
[6] Departamento de Física Teórica y del Cosmos, Facultad de Ciencias, Universidad de Granada, E-18071 Spain; simon@ugr.es
[7] Laboratoire d'Astrophysique de Bordeaux, Université Bordeaux, F-33270 Floirac, France; braine@obs.u-bordeaux1.fr
[8] Departamento Física Teórica y del Cosmos, Campus de Fuentenueva, Universidad de Granada, E-18071 Granada, Spain; mrelano@ugr.es
[9] Leiden Observatory, Leiden University, P.O. Box 9513, NL-2300 RA Leiden, The Netherlands; pvdwerf@strw.leidenuniv.nl
[10] Sterrewacht Leiden, Leiden University, P.O. Box 9513, 2300 RA Leiden, The Netherlands; israel@strw.leidenuniv.nl
[11] Departamento de Física Teórica y del Cosmos, Universidad de Granada, Spain; hermelo@iram.es
[12] Argelander-Institut für Astronomie, Auf dem Hügel 71, D-53121 Bonn, Germany; malbrecht@astro.uni-bonn.de
Received 2013 December 13; accepted 2014 February 19; published 2014 March 14

ABSTRACT

Infrared emission is an invaluable tool for quantifying star formation in galaxies. Because the 8 μm polycyclic aromatic hydrocarbon (PAH) emission has been found to correlate with other well-known star formation tracers, it has widely been used as a star formation rate (SFR) tracer. There are, however, studies that challenge the accuracy and reliability of the 8 μm emission as a SFR tracer. Our study, part of the *Herschel* (*Herschel* is an ESA space observatory with science instruments provided by European-led Principal Investigator consortia and with important participation from NASA) M33 Extended Survey (HERM33ES) open time key program, aims at addressing this issue by analyzing the infrared emission from the nearby spiral galaxy M33 at the high spatial scale of ~75 pc. Combining data from the *Herschel Space Observatory* and the *Spitzer Space Telescope*, we find that the 8 μm emission is better correlated with the 250 μm emission, which traces cold interstellar gas, than with the 24 μm emission. Furthermore, the $L(8)/L(250)$ ratio is more tightly correlated with the 3.6 μm emission, a tracer of evolved stellar populations and stellar mass, than with a combination of Hα and 24 μm emission, a tracer of SFR. The $L(8)/L(24)$ ratio is highly depressed in 24 μm luminous regions, which correlate with known H II regions. We also compare our results with the dust emission models by Draine & Li. We confirm that the depression of 8 μm PAH emission near star-forming regions is higher than what is predicted by models; this is possibly an effect of increased stellar radiation from young stars destroying the dust grains responsible for the 8 μm emission as already suggested by other authors. We find that the majority of the 8 μm emission is fully consistent with heating by the diffuse interstellar medium, similar to what recently determined for the dust emission in M31 by Draine et al. We also find that the fraction of 8 μm emission associated with the diffuse interstellar radiation field ranges between ~60% and 80% and is 40% larger than the diffuse fraction at 24 μm.

Key words: dust, extinction – galaxies: individual (M33) – galaxies: ISM – infrared: ISM – Local Group

Online-only material: color figures

1. INTRODUCTION

In order to understand the evolution of galaxies in the Universe, accurate measures of star formation within galactic structures need to be obtained. A large number of tracers of star formation in a galaxy have been defined in the literature, using different regions of the electromagnetic spectrum. Among these, the infrared (IR) radiation is a classical tracer of activity in galaxies (Kennicutt 1998; Kennicutt & Evans 2012; Calzetti 2012). In star-forming galaxies, young, massive stars are responsible for most of the ultraviolet (UV) radiation and, in the presence of dust a smaller or larger fraction of their light may be absorbed and reradiated in the IR regime. By observing galaxies in IR light, determinations about the rate and areas of star formation can be surmised.

The mid-IR wavelength region (≈7–40 μm) in general and the emission around ~8 μm in particular are among the favored tracers of recent star formation, because of their ready detectability in galaxies at high redshift (e.g., Daddi et al. 2005; Reddy et al. 2010, 2012). The emission in the ~8 μm region is mainly contributed by a combination of stellar photospheric emission, the featureless continuum of hot dust emission, and the polycyclic aromatic hydrocarbon (PAH) spectral features (e.g., Smith et al. 2007). As the PAH features contribute about 70% or more of the emission in the *Spitzer* ~8 μm band (Smith et al. 2007), we call the emission in this band "PAH emission" henceforth. Roussel et al. (2001) and Förster Schreiber et al. (2004) have suggested, using data from the *Infrared Space Observatory*, that the PAH emission is closely related to the hot dust emission at 15 μm and other tracers of star formation. Other studies (e.g., Boselli et al. 2004; Haas et al. 2002) and follow up investigations, utilizing the *Spitzer Space Telescope* (Werner et al. 2004), found the relation to be more complex than previously inferred. The PAH emission does not immediately

correlate with star formation as traced by the 24 μm emission, as the $L(8)/L(24)$ luminosity ratio is depressed in regions of known star formation relative to the ratio in the diffuse starlight field (Helou et al. 2004; Calzetti et al. 2005; Bendo et al. 2008; Povich et al. 2007). Bendo et al. (2006, 2008), furthermore, showed that the PAH emission is more closely related to tracers of cool dust emission, heated by the diffuse starlight field, than tracers of warm dust, heated by recent star formation. This is confirmed by Verley et al. (2009), who used a complementary approach to our own to determine that at least 60% of the 8 and 24 μm emission in M33 is diffuse. Conversely, a recent study by Crocker et al. (2013) determined that the 8 μm emission in the galaxy NGC 628 has only a 30%–43% fraction unassociated with recent star formation. These contradictory results call for further studies to assess the validity of the PAH emission as a star formation rate (SFR) tracer.

The powerful *Herschel Space Observatory* (Pilbratt et al. 2010) has targeted nearby galaxies with unprecedented resolution at the infrared wavelengths ($\geqslant$70 μm) where the warm dust emission, powered primarily by massive stars, is progressively supplanted by the cold dust emission powered by low mass stars (Bendo et al. 2010, 2012; Boquien et al. 2011). The synergy between the *Spitzer* and *Herschel* imaging data is such that the infrared spectral energy distribution of individual star forming regions from $\sim$3 μm to the submillimeter can be separated from that of the diffuse starlight in nearby galaxies, permitting perusal of the emission originating in these regions. With this level of detail, the properties of dust emission and its relation to the SFR can be better investigated. This paper uses data from both *Spitzer* and *Herschel* to observe the nearby galaxy, M33, in a range of IR wavelengths.

M33 is a member of the Local Group and a spiral galaxy, with an inclination of 56° (Regan et al. 1994) and a distance of 840 kpc (Freedman et al. 1991). Because of its proximity, M33 is an ideal site for the investigation of the properties of dust emission: 1″ subtends a spatial scale of $\sim$4 pc. M33 harbors a large number of H II regions (Boulesteix et al. 1974; Hodge et al. 1999; Verley et al. 2010; Relaño et al. 2013), which are easily identifiable in the *Spitzer* and *Herschel* images. M33 has an oxygen abundance of about half solar and a shallow-to-negligible metallicity gradient as a function of galactocentric distance (Rosolowsky & Simon 2008; Magrini et al. 2009; Bresolin 2011); this characteristic enables us to investigate the PAH emission with less attention to the effect of metallicity on the strength of the PAH features (Hunt et al. 2005; Engelbracht et al. 2005; Madden et al. 2006; Draine et al. 2007; Engelbracht et al. 2008). The *Herschel* data for this project came from the HERM33ES open time key program (Kramer et al. 2010) and *Spitzer* data were obtained through the Guaranteed Time observations for the IRAC and MIPS instruments (Hinz et al. 2004; McQuinn et al. 2007). We also make use of the Hα image from Hoopes & Walterbos (2000), taken with the 0.6 meter Burrell-Schmidt telescope at Kitt Peak National Observatory. Details about the imaging and its reduction can be found in that paper.

Relationships among the PAH 8 μm, 24 μm, 250 μm, and total infrared (TIR) emission are the primary subjects of this study, under the reasonable assumption that the 24 μm emission is mainly tracing current star formation (Calzetti et al. 2005, 2007) and that the 250 μm emission is mainly tracing cold dust.

Our analysis plan is similar to that used by Bendo et al. (2008) for the SINGS galaxies (Kennicutt et al. 2003): we will investigate the relationship of the 8 μm emission with tracers of the warm (24 μm) and cool (250 μm) dust emission, and with the TIR emission. The advantage of our analysis over that of Bendo et al. is twofold: (1) M33 is 3–20 times closer than the SINGS galaxies, thus enabling exquisite spatial resolution; and (2) the 250 μm emission from *Herschel* traces more closely the cool dust and has more than twice the spatial resolution of the 160 μm *Spitzer* data used by Bendo et al.

In what follows, $L(\lambda)$ refers to monochromatic luminosity derived as

$$L(\lambda) = [\nu L_\nu]_\lambda \quad (1)$$

in units of erg s^{-1} kpc^{-2}. In this work, each pixel will be $\sim$73.3 pc in size, or about the size of a large H II region.

2. DATA

This study makes use of mosaics of M33 obtained in the following bands: 3.6, 8, 24, 70, 160, and 250 μm. Figure 1 shows luminosity maps of 3.6, 8, 24, and 250 μm images. The 3.6, 8, 24, and 70 μm images were obtained with the Infrared Array Camera (IRAC for 3.6 and 8 μm; Fazio et al. 2004) and the Multiband Imaging Photometer for *Spitzer* (MIPS for 24 and 70 μm; Rieke et al. 2004) instruments on the *Spitzer Space Telescope* (Werner et al. 2004). The point-spread function (PSF) of the images ranges from $\sim$2″ to $\sim$18″. The 3.6 μm image mainly contains photospheric emission from stars (Meidt et al. 2012), and was used to subtract stellar contributions in the 8 and 24 μm images.

Emission at 24 μm in nearby galaxies comes primarily from hot dust ($\gtrsim$100 K), and becomes luminous more rapidly than other IR bands in strong radiation fields, such as star forming regions (Draine & Li 2007). It has been calibrated as a SFR tracer, either by itself or in combination with Hα (Alonso-Herrero et al. 2006; Calzetti et al. 2005, 2007). Emission at 70 μm is also a reasonable tracer of star forming regions in luminous galaxies, as it accounts for a significant fraction of the total IR emission ($\sim$30%–50%; Calzetti et al. 2010; Boquien et al. 2010; Li et al. 2010, 2013). The 160 μm image was obtained using the Photodetector Array Camera and Spectrometer (PACS; Poglitsch et al. 2010) on the *Herschel Space Observatory* (Pilbratt et al. 2010). These bands were used to derive the TIR image of M33, as they trace the bulk of the total infrared emission. The 250 μm image was obtained using the Spectral and Photometric Imaging Receiver (SPIRE; Griffin et al. 2010) on *Herschel*. For more details about the reduction and nature of the data, see Kramer et al. (2010), Verley et al. (2010), and Boquien et al. (2011).

The images were convolved to the PSF of the 250 μm image, 19.″7 $\pm$ 1.″7 (Kramer et al. 2010). This was done using a convolution script in IDL and kernels from Aniano et al. (2011). Using Fourier transformations, this process takes an image, resamples it, and resizes it to match a reference kernel. When this was completed, the image was aligned to the 250 μm image. Thus, all images used for our analysis were processed to be at the same pixel size, aligned with, and with the same field of view as the 250 μm image.

Next, we subtracted the stellar component of the infrared emission in the 8 and 24 μm bands. In order to find the optimal factor of the 3.6 μm emission to subtract, the fluxes of 50 point sources (foreground stars) were measured in all three images: 3.6, 8, and 24 μm. Histograms of the 8/3.6 and 24/3.6 flux ratios were used to identify the peak ratio value, to be used as initial guess for the optimal fraction of the 3.6 μm fluxes to be subtracted from each of the 8 and 24 μm images, respectively. With these initial guesses, we produced several images with

2. Data

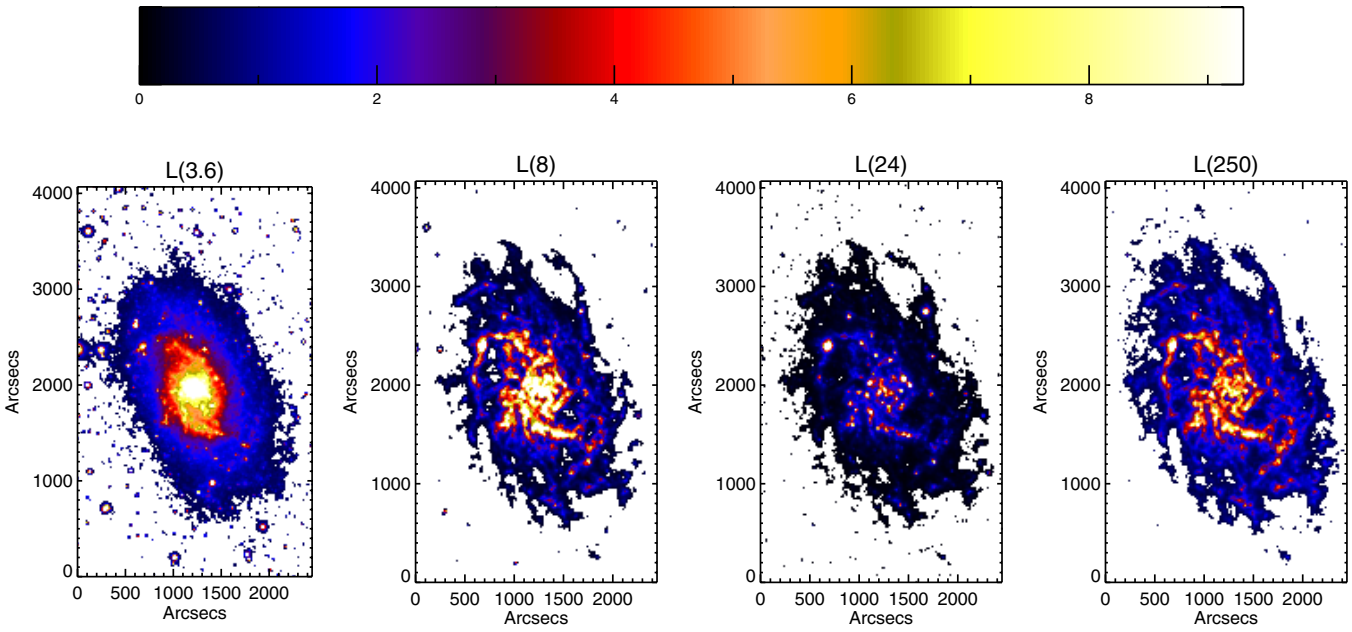

Figure 1. Luminosity maps at 3.6, 8, 24, and 250 μm. Each map has been convolved to the 250 μm resolution (PSF = 19.″7) and resampled in bins of 18″ × 18″. The units of the color bar are 10^{40} erg s^{-1} kpc^{-2}.

(A color version of this figure is available in the online journal.)

varying degrees of stellar subtraction, which were compared to establish the fractions of 3.6 μm fluxes that would yield the least amount of stellar residual, while at the same time avoiding over-subtraction in the regions of diffuse emission. We found these fractions to be 0.35 for the 8 μm image and 0.06 for the 24 μm image, with all images still in units of MJy sr^{-1}. Although these fractions are larger than those derived by Helou et al (2004) and Calzetti et al. (2007), they are consistent with expectations from stellar population synthesis models with star formation durations ≈1 Gyr or longer (Leitherer et al. 1999). Choosing Helou et al.'s (2004) factor of 0.25 for the rescaling of the 3.6 μm image, instead of our derived 0.35, changes the measured 8 μm fluxes by 8% on average, as derived from the mode of the ratio of the two 8 μm images. Furthermore, we performed checks on the stellar-continuum subtracted 8 and 24 μm images at the original (non-convolved) resolution, to verify that the subtraction of the 3.6 μm image is effective at removing also the contribution of foreground stars that are located within the extent of the galaxy, while ensuring that no region is over-subtracted.

In order to improve signal-to-noise ratio (S/N), the images were rebinned to be pixels 18″ on a side. At the distance of M33, this angular resolution corresponds to a spatial scale of 73 pc, which is the size of a large H II region. Thus, our re-binning of the images does not impact our results, since we can still easily separate regions dominated by young stars from more quiescent regions. Rebinning to the size of the 250 μm PSF also makes our pixels independent.

After stellar subtraction and rebinning, sky background was removed from all images, using the msky procedure available in IRAF,[13] which calculates the mode and the standard deviation of the average pixel values. We use the standard deviation as our 1σ value for that band. Only fluxes above the 5σ level are used in the sky subtracted images to ensure that measurements are significant; with this threshold selection, we usually have at least 4500 separate pixels in each of the images.

Extended source aperture corrections were applied to the 3.6 and 8 μm data due to the extended nature of the features in M33. To account for this, the 3.6 μm flux was multiplied by a constant of 0.96 and the 8 μm flux was multiplied by a constant of 0.81, consistent with the correction to an infinite aperture photometry of our pixel photometry, as found in the *IRAC* Instrument Handbook.[14]

A TIR surface brightness image was produced for comparison with the monochromatic images and ratio images. Following the prescription of Dale & Helou (2002), the single-band images of M33 are added to produce a TIR image in the following way:

$$L_{(\mathrm{TIR})} = 1.559L(24) + 0.7686L(70) + 1.347L(160), \quad (2)$$

where $L(\lambda)$ is defined as in Equation (1). The luminosities determined in Equation (1) are found to be in agreement with those determined using a more extensive range in fluxes, as derived in Boquien et al. (2011) paper, typically within 4%–5% in all bins with a dispersion of 5%–10%. The recipe given in Draine & Li (2007) Equation (22), is similar to Equation (2) above, but includes the 8 μm emission in the TIR estimate. Comparisons between maps using our Equation (2) and the Draine & Li (2007) estimator show a systematic offset of 8% (Equation (2) giving a lower TIR estimate) with a dispersion of 7%. Given the similarity of all estimators and the absence of systematic differential trends across the galaxy, we adopt Equation (2) for our analysis. Figure 2 shows the TIR luminosity map of the galaxy. In this figure, the TIR maps shows a larger fraction of bins below our S/N = 5 cut than any of the images shown in Figure 1. This is due to the use of the lower S/N map at 160 μm from *Herschel*/PACS to produce the TIR image.

[13] Dr. Mark Dickinson, NOAO (1998, private communication).

[14] irsa.ipac.caltech.edu/data/SPITZER/docs/irac/iracinstrumenthandbook/

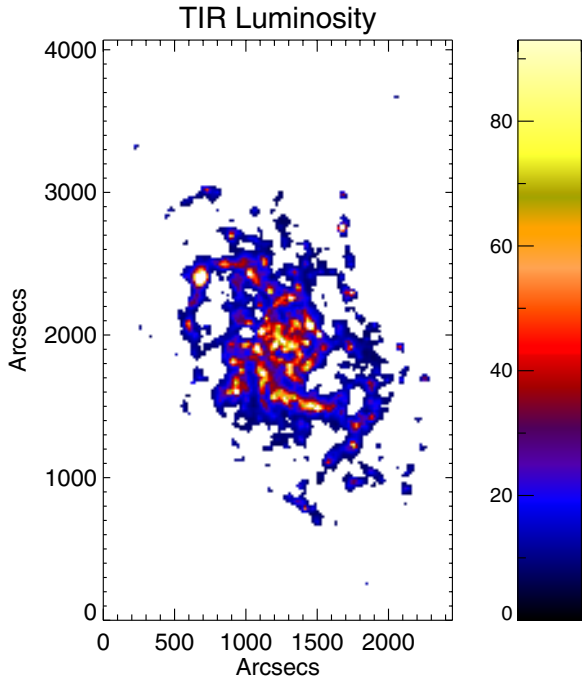

Figure 2. TIR Luminosity map image. The resolution of the image is the same as that reported in Figure 1. The units of the color bar are 10^{40} erg s^{-1} kpc^{-2}.
(A color version of this figure is available in the online journal.)

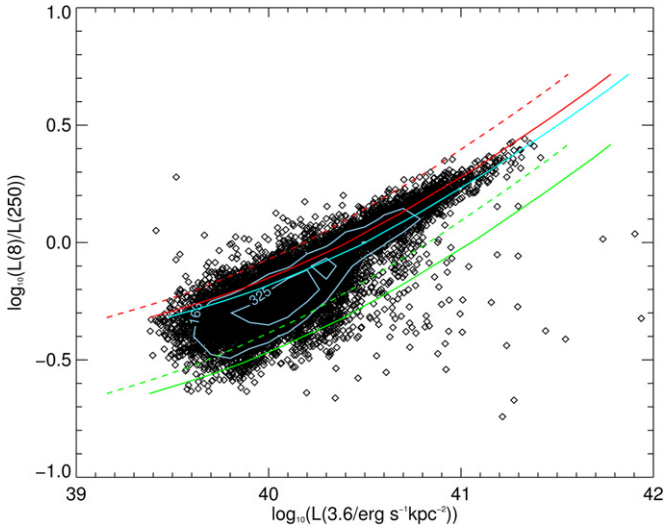

Figure 3. Scatter plot showing $L(8)/L(250)$ luminosity ratio vs. $L(3.6)$, the stellar luminosity in the 3.6 μm IRAC band for the pixels in the M33 images. The red line is the Draine & Li (2007) $q_{\rm PAH} = 0.046$ model with an f factor of 1.25 (solid line, see Equation (3)) and 0.75 (dashed line), respectively. The green line is the 2.5% PAH mass fraction case with an f factor of 1.25 (solid line, see Equation (3)) and 0.75 (dashed line), respectively. The f value and PAH mass fraction adopted in this paper is shown as the solid cyan line, $q_{\rm PAH} = 0.046$ with $f = 1.55$. Models are plotted for $U_{\rm min} = U_{\rm max}$ (single-valued ISRF), where $U_{\rm min}$ covers the range 0.1–25. Contours in all figures report the number of points within a contour region. The model $L(3.6)$ is calculated as described in Section 3.2.
(A color version of this figure is available in the online journal.)

3. ANALYSIS

3.1. Models

We compare our data with the dust emissivity models of Draine & Li (2007). Briefly, these are physically motivated models that describe the heating of dust by starlight, where the dust is a mixture of amorphous silicate and graphitic grains, including PAH particles. The fraction of PAHs present in the models is a parameter called $q_{\rm PAH}$, which is the percentage by mass of PAHs relative to the total dust mass. A number of authors (Hunt et al. 2005; Engelbracht et al. 2005; Madden et al. 2006; Draine et al. 2007; Smith et al. 2007; Engelbracht et al. 2008) have established that above a critical metallicity value of about 20% solar, the value of $q_{\rm PAH}$ is relatively constant, and close to the Milky Way (MW) value of 0.04. Here, we adopt the closest value for which models are available, $q_{\rm PAH} = 0.046$, as our default for M33, on account of this galaxy being only about 0.5 solar in metal abundance. In some cases, for comparison, we also present the $q_{\rm PAH} = 0.025$ models. This is noted in the figure captions.

In the Draine & Li (2007) models, the starlight intensity heating the dust is modeled as a dimensionless factor U that multiplies the general interstellar radiation field (ISRF) in the solar neighborhood, as estimated by Mathis et al. (1983). In order to account for the range of starlight intensities present in galaxies, these authors parameterize the starlight as the sum of two contributions: one describing the ISRF of the galaxy, with dimensionless factor $U_{\rm min}$, and the other describing regions of higher starlight intensity, with U varying between $U_{\rm min}$ and $U_{\rm max}$. The latter factor accounts for the heating of dust by the increasingly higher stellar energy densities in the proximity of OB associations and other high energy regions, where $U > 100$. More details on the models, and the predicted dust emission intensity in the various *Spitzer* and *Herschel* bands can be found in the original paper (Draine & Li 2007). Here we will compare our spatially resolved data of M33 with these models, for varying $U_{\rm min}$ and $U_{\rm max}$.

We perform comparisons using both luminosity ratios (e.g., $L(8)/L(24)$) and luminosities (e.g., $L(3.6)$, $L(24)$, etc.). Luminosity ratios are readily available from the models, while the model luminosities need to be derived for our specific case (distance, region size, etc.). The model stellar luminosity at 3.6 μm is obtained assuming that the ISRF spectrum of Mathis et al. (1983) for the solar neighborhood is applicable to M33. We rescale this spectrum to the distance of M33 and our region sizes of 73.3 pc. In order to account for the fact that we are observing M33 from an external vantage point, rather than from within the galaxy itself (as if the case for the Milk Way), we model the galaxy as a plane parallel homogeneous distribution of stars and dust, with inclination of 56°, yielding the following "net" expression for the 3.6 μm luminosity per pixel:

$$L(3.6) = \langle U \rangle \times f \times 1.922 \times 10^{40} \ \ {\rm erg\,s^{-1}\,kpc^{-2}}, \qquad (3)$$

where $\langle U \rangle$ is the mean value of the starlight intensity in the pixel, and f is a factor that accounts for variations in the dust optical depth (thus, gas column densities) in the disk. For a metal abundance about 0.5 solar and a total gas, H I + H_2, gas column density in the range 4×10^{20} to 6×10^{21} cm^{-2} (Gratier et al. 2010; Braine et al. 2010), f is in the range [0.75; 1.25]. See the Appendix for the derivation of Equation (3). Figure 3 shows the scatter plot of $L(8)/L(250)$ versus $L(3.6)$ for the M33 pixels,[15] with the expectations from the Draine & Li (2007) model overlaid, for $f = 0.75$ and $f = 1.25$; for the model,

[15] In producing the plots that follow, it was found that the 5σ boundaries on the emission ratios usually lay far from the data points themselves. In this case, the 5σ lines do not provide a selection bias. For this reason, we have chosen to plot the 5σ boundaries only in the cases for which they provide a selection limit on the data.

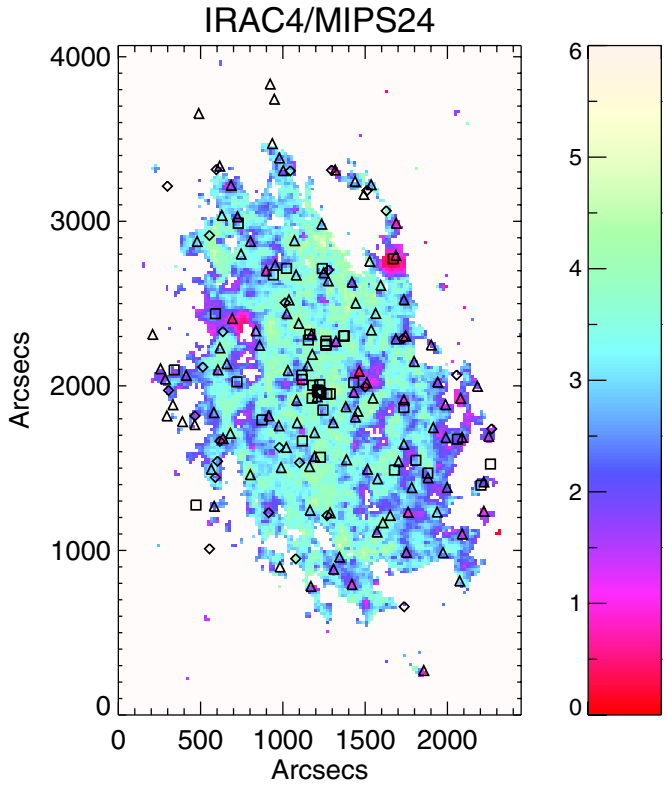

Figure 4. Ratio image of $L(8)/L(24)$ luminosity. The resolution of the image is the same as that reported in Figure 1. Prominent H II regions are identified in the image; 27 regions from Verley et al. (2007) are denoted by diamonds, 119 regions from Relaño et al. (2013) are denoted by triangles, and 39 of the brightest H II regions from Hodge et al. (1999) are denoted by squares. H II regions tend to cluster close to the minima in the $L(8)/L(24)$ ratio.

(A color version of this figure is available in the online journal.)

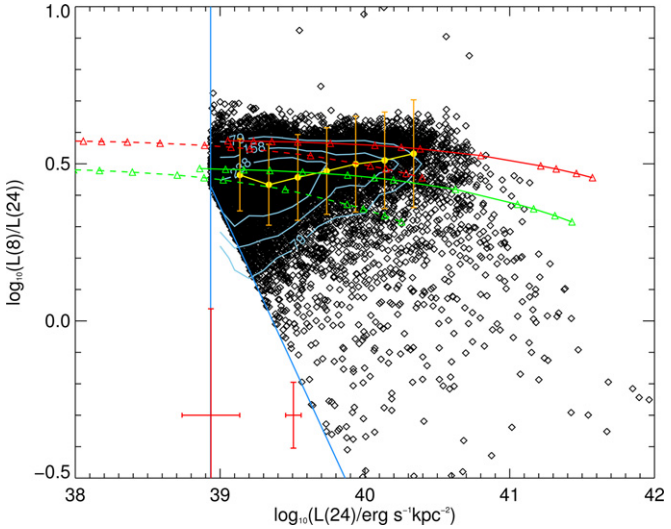

Figure 5. Ratio of $L(8)/L(24)$ vs. 24 μm luminosity plot. Blue lines mark the 5σ limit on the data. The median values of the data are presented as the yellow points and line, with dispersion bars at each point the median was calculated. The predicted values for the emissivity from Draine & Li (2007) for the $q_{\rm PAH} = 0.046$ case (red lines; Section 3.2) and the $q_{\rm PAH} = 0.025$ case (green lines), are plotted for $U_{\rm min} = U_{\rm max}$ in the range 0.1–25. Dashed lines are models calculated using an $N_{\rm H}$ of 4×10^{20} cm^{-2} and solid lines are models calculated using an $N_{\rm H}$ of 6×10^{21} cm^{-2}. Representative red 1σ uncertainty bars on the data are presented at the bottom of the plot.

(A color version of this figure is available in the online journal.)

we adopt both $q_{\rm PAH} = 0.046$ (see above) and the lower value $q_{\rm PAH} = 0.025$ for completeness. We allow $\langle U \rangle = U_{\rm min}$ to span the range 0.1–25. This range is in agreement with what Draine et al. (2014) find for the Andromeda galaxy. We find a small offset in Figure 3 between the $q_{\rm PAH} = 0.046$ model and the data, which can be caused by any number of the following reasons: (1) the ISRF spectrum of M33 may differ from that of the MW; (2) the dust and stars are not homogeneously distributed across the disk; (3) dust and stars may have different scale heights in the galaxy, and these scales may also depend of the mean stellar population age; or (4) the fraction of PAHs, $q_{\rm PAH}$, in M33 may be slightly different (lower) from that of the MW, although our data do not have the accuracy to enable an exact determination of this parameter. As in the case of $L(3.6)$, the dust luminosities depend on both the starlight intensity $\langle U \rangle$ (Draine & Li 2007) and the range of gas column densities (dust opacities) parameterized by the factor f, which we adopt to have fixed value $f \sim 1.55$. Thus, for the purpose of this analysis, we adopt $q_{\rm PAH} = 0.046$ and a mean value of f that approximately matches the data in Figure 3, $f \sim 1.55$, and keep it constant in the rest of the paper. Where relevant, we also show the case $q_{\rm PAH} = 0.025$.

The model dust luminosities, $L(8)$, $L(24)$, $L(250)$, etc., are derived by converting the emissivity per unit H atom to a total emissivity per pixel by using the range of H I + H_2 column densities given above, after multiplying said emissivity by 0.5 to account for the roughly half solar metallicity of M33, and recalling that each pixel in our analysis subtends 73.3 pc. As in the case of $L(3.6)$, the dust luminosities are also parameterized by $\langle U \rangle$, and are multiplied by the same factor $f \sim 1.55$. In order to account for the range of gas column densities observed in M33, we show in all relevant figures the model dust luminosities derived under the two extreme assumptions of N(H I+H_2) = 6×10^{21} cm^{-2} and N(H I+H_2) = 4×10^{20} cm^{-2}.

3.2. Relationships between 8 μm and 24 μm Emission

Figure 4 shows the ratio map of $L(8)/L(24)$ luminosity of the galaxy. The ratio is somewhat homogenous over the galaxy, with minima in documented H II regions (Hodge et al. 1999; Verley et al. 2007; Relaño et al. 2013). One prominent example is seen in the upper right arm, where a large minimum is present. This minimum correlates with a luminous region in the 70 μm image, which traces star forming regions. The presence of $L(8)/L(24)$ ratio minima in H II regions indicates that 8 μm emission is under luminous within H II regions, as already noted by Helou et al. (2004) in the galaxy NGC 300 and Povich et al. (2007) in the MW H II region M17. This trend is better seen in Figure 5, where the $L(8)/L(24)$ luminosity ratio is plotted as a function of the 24 μm luminosity (in each pixel), showing that luminous regions correspond to low $L(8)/L(24)$ ratio values.

In Figure 5, a generally flat trend of the data is evident, confirmed by the running median of the data points. This is consistent with the range of slopes found in other galaxies analyzed by Bendo et al. (2008). In their paper, such a relationship as is found in M33 was taken to imply a dissociation between the 8 and 24 μm emission. One difference between our findings and those of Bendo et al. should be noted, however. In their paper, they report a systematically decreasing trend of the 8/24 ratio for all 24 μm surface brightnesses, even at the faintest level. This disparity between our results and those of Bendo likely stems from our much improved spatial resolution (73 pc versus the typical 550 pc of Bendo et al., i.e., a factor 7.5 better spatial resolution), that enables us to cleanly separate regions of current star formation from the more quiescent regions.

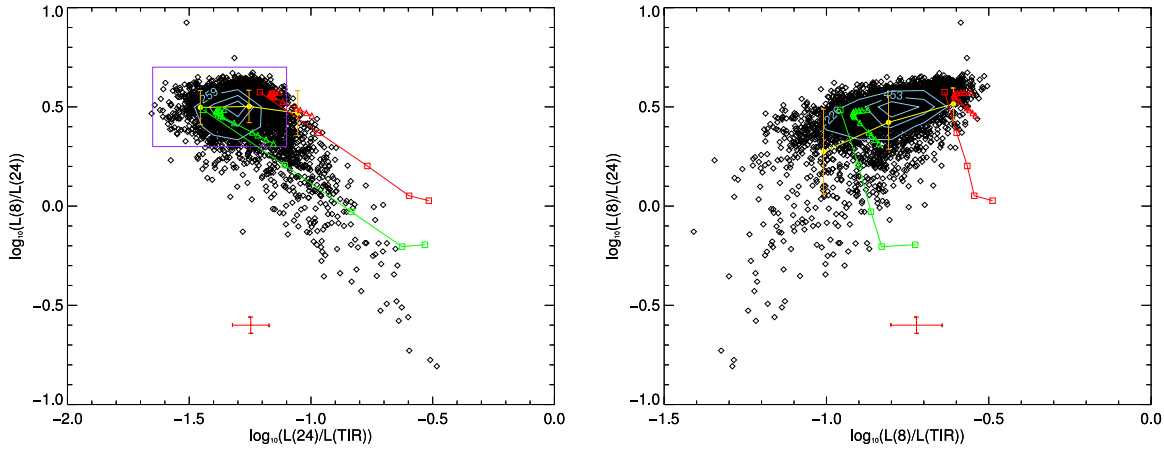

Figure 6. Relation between the $L(8)/L(24)$ and the $L(24)/L(\mathrm{TIR})$ and $L(8)/L(\mathrm{TIR})$ ratios. The median values of the data are presented as the yellow points and line, with dispersion bars at each point the median was calculated. The predicted values for the emissivity from Draine & Li (2007) for the $q_{\mathrm{PAH}} = 0.046$ case (red lines; Section 3.2) and the $q_{\mathrm{PAH}} = 0.025$ case (green lines), are plotted for both $U_{\mathrm{min}} = U_{\mathrm{max}}$ in the range 0.1–25 (triangle points) and $U_{\mathrm{min}} = 0.1$ with U_{max} ranging from 0.1 to 10^6 (square points). The purple box in the left panel demarcates the area used for the calculation of diffuse fractions (see Section 4).

(A color version of this figure is available in the online journal.)

Our data are flatter overall until a $\log_{10}(L(24)/\mathrm{erg\ s^{-1}\ kpc^{-2}})$ value of ∼40.65, after which a sharp decline in the $L(8)/L(24)$ ratio occurs. For our resolution, this corresponds to a total 24 μm luminosity of 2.1×10^{38} erg s^{-1}, which would correspond to an Hα luminosity of 6.5×10^{36} erg s^{-1}, when using Equation (5) of Calzetti et al. 2007. This is the H α luminosity of an H II region powered by a 5 Myr old star cluster with mass of about 800 $M_{\odot}$ (Starburst99 models; Leitherer et al. 1999). These are some of the smallest star clusters that can dominate the emission within regions of 70 pc size.

The models over-plotted on the data are for both cases of $q_{\mathrm{PAH}} = 0.046$ and $q_{\mathrm{PAH}} = 0.025$ with $U_{\mathrm{min}} = U_{\mathrm{max}}$ and ranges from 0.1 to 25. Two different line styles are shown in Figure 5, corresponding to two different assumptions for the column density of total hydrogen in M33. Values for N_{H} are from the column density maps of Gratier et al. (2010) and Braine et al. (2010), which describe an approximate range of N_{H} from 4×10^{20}–6×10^{21}.

Additional insights can be obtained by plotting the $L(8)/L(24)$ ratio as a function of the $L(8)/L(\mathrm{TIR})$ and $L(24)/L(\mathrm{TIR})$ ratios. In this case, the observed data can be compared directly with predictions from models. Figure 6 shows the observed $L(8)/L(24)$ versus $L(24)/L(\mathrm{TIR})$ and $L(8)/L(\mathrm{TIR})$.

The $L(8)/L(24)$ ratio as a function of the $L(24)/L(\mathrm{TIR})$ ratio shows that the 8 μm luminosity is low relative to the 24 μm in areas of high 24 μm luminosity. The second ratio plot as a function of $L(8)/L(\mathrm{TIR})$ confirms this, and implies that 8 μm emission is under luminous in areas of high star formation. We quantify this statement by calculating the fraction with low $L(8)/L(24)$ within 150 pc of the 119 H II regions from Relaño et al. (2013). We find that for all pixels below $\log(L(8)/L(24)) = 0.15$ (about 3.5% of all pixels above 5σ), 60% of them are located within 150 pc of an H II region. Conversely, when considering pixels with $\log(L(8)/L(24)) \geqslant 0.15$, only 18% of them are within 150 pc of one of Relaño et al.'s H II regions. These fractions do not change when choosing different thresholds for $\log(L(8)/L(24))$, as long as they are $\leqslant 0.2$. This ratio corresponds to a starlight intensity of $U \approx 10^2$ (Draine & Li 2007) for most q_{PAH} values. When analyzing independently the $L(8)/L(\mathrm{TIR})$ and $L(24)/L(\mathrm{TIR})$ as a function of distance from H II regions, we find that while $L(8)/L(\mathrm{TIR})$ is roughly constant or slightly decreasing in value when approaching an H II region, $L(24)/L(\mathrm{TIR})$ shows an increase, thus confirming the $L(8)/L(24)$ trend. This can also be seen in Figure 7, where we plot the fraction of pixels within distance R from the nearest H II region and with $L(8)/L(\mathrm{TIR})$ below a certain value (X) versus the distance. For $L(8)/L(\mathrm{TIR}) < 0.063$ ($\log(L(8)/L(\mathrm{TIR}) < -1.2$, see Figure 6, right panel), the $L(8)/L(\mathrm{TIR})$ ratio is higher closer to an H II region, implying that low values of $L(8)/L(\mathrm{TIR})$ tend to cluster close to H II regions. As X increases, there are two effects: the absolute value of the ratio increases and tends toward unity (as expected, since now we include a larger range of values for $L(8)/L(\mathrm{TIR})$), and the trend as a function of increasing radius disappears, which is also expected if large values of $L(8)/L(\mathrm{TIR})$ can be both close and far from H II regions. This is due to the fact that, even in a pixel containing an H II region, much of the IR emission is from dust located along the line of sight and not directly associated with the H II region; only in correspondence of a bright H II region we can expect a measurable effect on the overall 8 μm emission from the pixel. This reinforces the conclusions based on $L(8)/L(24)$: low values of 8 μm surface brightness tend to be closer to H II regions.

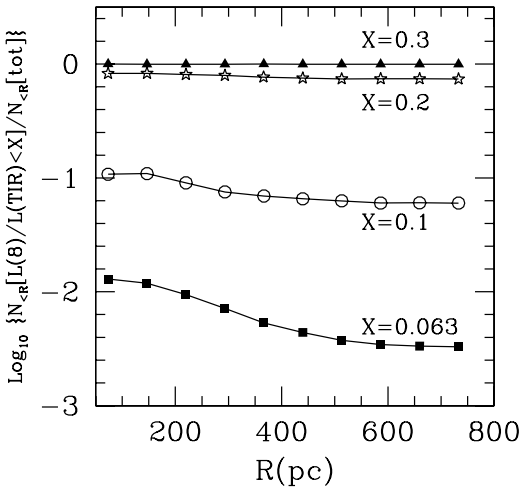

Figure 7. Fraction of pixels within distance R with $L(8)/L(\mathrm{TIR})$ below a certain value (X) as a function of distance from the nearest H II region.

The 8 μm emission is underluminous relative to expectations from models that include heating from H II regions (exemplified

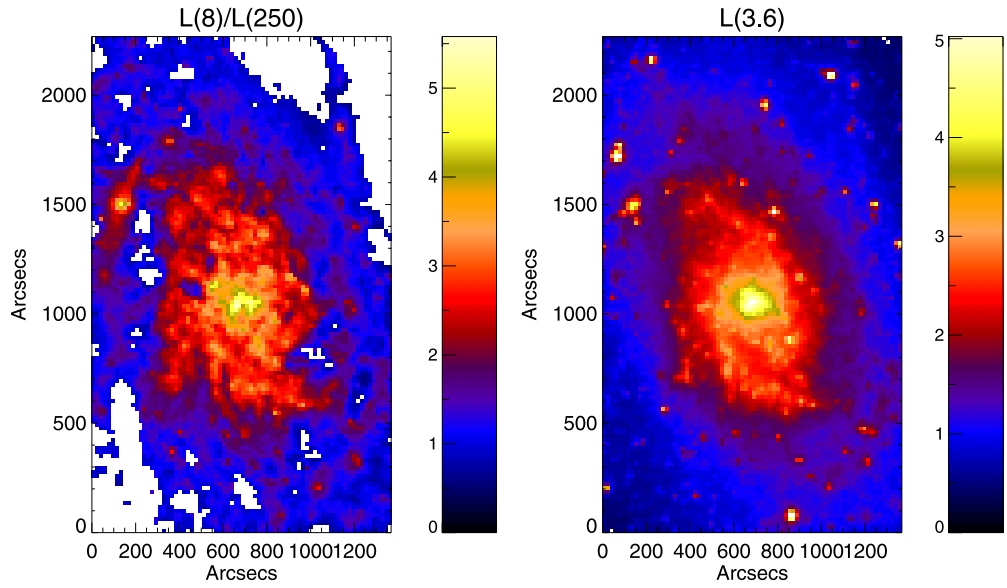

Figure 8. Ratio image of $L(8)/L(250)$ luminosity. Resolution is detailed in the caption of Figure 4. For comparison, the 3.6 μm map is presented on the right; the units of the color bar for the $L(3.6)$ image are 10^{40} erg s^{-1} kpc^{-2}. The similar radial trends inherent in both the $L(8)/L(250)$ ratio and 3.6 μm images suggests that the 8 μm emission traces the same old stellar population as the 3.6 μm emission.

(A color version of this figure is available in the online journal.)

here adopting $U_{\rm max} \approx 10^6$ in the Draine & Li 2007 models, as suggested by those authors). This supports earlier findings and suggestions that the PAH carriers tend to be destroyed in regions of high starlight intensity (Helou et al. 2004; Bendo et al. 2008; Povich et al. 2007; Gordon et al. 2008).

3.3. Relationships between 8 μm and 250 μm Emission

An interesting comparison of the $L(8)/L(250)$ ratio with the old stellar population, traced with the 3.6 μm emission, suggests that the PAH actually traces old stars. Figure 8 shows the ratio image next to the 3.6 μm image; which shows strong similarity. Figure 9 compares the galactocentric trends more quantitatively through elliptical summations of signal as a function of radius. The presence of a galactocentric gradient in $L(8)/L(250)$ suggests the $L(8)$ increases toward the center of M33 faster than $L(250)$ does. Although not shown, we find a similar result for $L(8)/L(\rm TIR)$, which indicates that the trend in $L(8)/L(250)$ is not due to changes in the thermal peak of the dust emission. This trend is likely an indication of a closer correlation of $L(8)$ to the ISRF heating as traced by the 3.6 μm emission than to star formation or young stellar population tracers.

Figure 10 shows the relation of the $L(8)/L(250)$ ratio with the 250 μm surface brightness. The plot shows a positive slope, suggesting that the 8 μm brightness increases more than the 250 μm brightness as the latter becomes more luminous, with no evidence of a change in trend (a decrease), as found in the $L(8)/L(24)$ versus $L(24)$ scatter plot.

The slope obtained in our data is higher than that obtained by Bendo et al. (2008), but this is explained by the fact that our resolution allows for more accurate tracing of cold dust. We also use a longer wavelength tracer of cold dust then these authors (250 μm as opposed to 160 μm) implying that we are further along the Rayleigh-Jeans tail of the dust emission. The range spanned by the data is fully accounted for by the diffuse ISRF with $U_{\rm min}$ in the range 0.1–25. From Figure 10, we infer that the correlation of the PAH emission with cold dust is stronger than with star forming regions.

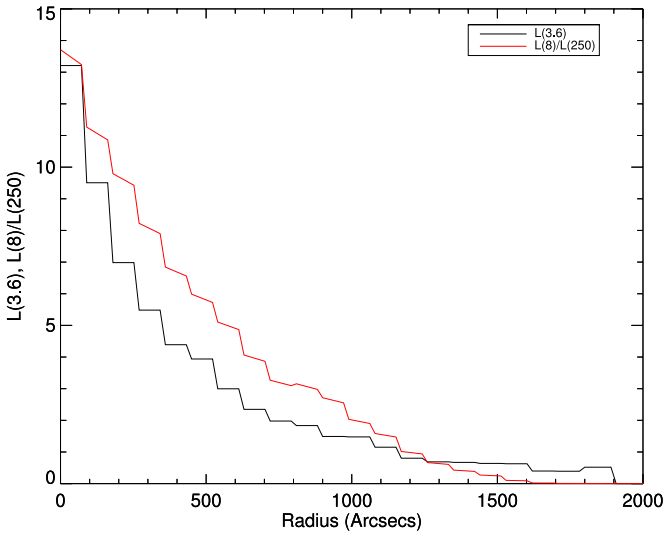

Figure 9. Azimuthally averaged galactocentric trends for both $L(8)/L(250)$ and $L(3.6)$, where $L(8)/L(250)$ have been scaled in the vertical direction by 3 to match the central value of $L(3.6)$. This plot aims at highlighting the similarities in the two trends, as also shown by the two panels of Figure 8. The values for the 3.6 μm emission are in black, while the ratio is represented by the red line. Units for the 3.6 μm luminosity are 10^{40} erg s^{-1} kpc^{-2}.

(A color version of this figure is available in the online journal.)

This is reinforced by the scatter plot of the $L(8)/L(250)$ ratio as a function of the TIR luminosity (not shown, but qualitatively similar to Figure 10), which we find to still show a strong increase of $L(8)/L(250)$ with $L(\rm TIR)$. This reinforces our earlier conclusion that while the PAH emission increases with the ISRF intensity more than the 250 μm emission, this trend is not due to a shift of the thermal peak of the dust emission to higher temperatures.

A very tight correlation can be found by plotting the $L(8)/L(250)$ ratio as a function of 3.6 μm luminosity, as in Figure 11. The marked decrease in scatter for $L(3.6) > 3.2 \times 10^{40}$ erg s^{-1} kpc^{-2}, by almost a factor of two, provides further

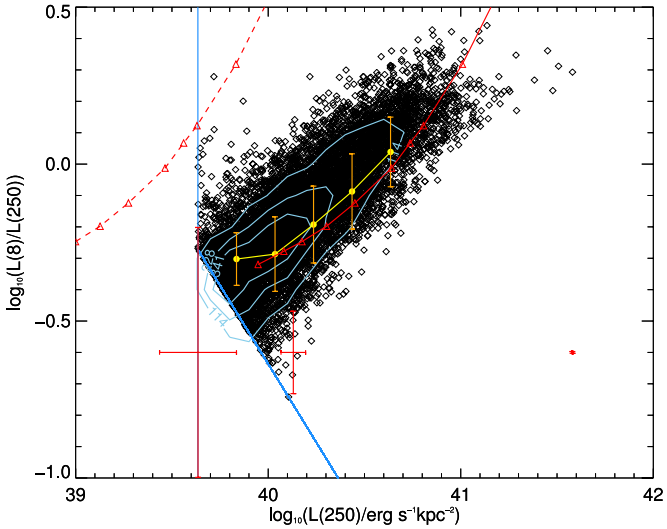

Figure 10. Ratio of $L(8)/L(250)$ vs. 250 μm luminosity. Plot symbols and colors are the same as those in Figure 5 for the $q_{\rm PAH} = 0.046$ model.

(A color version of this figure is available in the online journal.)

support for the statement that $L(8)/L(250)$ emission is strongly correlated with 3.6 μm emission, which is a tracer of old stellar populations. A histogram of the residuals of a best fit line through the data quantifies the dispersion (right panel of Figure 11). The blue histogram shows the dispersion of all data points in the left plot, while the red histogram shows the dispersion of all data above $L(3.6) = 3.2 \times 10^{40}$ erg s^{-1} kpc^{-2}. Gaussian fits to the histograms give FWHMs that decrease from 0.19 for all data to 0.11 for the bright $L(3.6)$ points, almost a factor of two decrease.

When we plot the $L(8)/L(250)$ ratio as a function of the combined luminosity of Hα and 24 μm emission, which is an accurate SFR indicator (Calzetti et al. 2007), as in Figure 12, we still find a correlation, but not as good as that found in Figure 11, with the 3.6 μm emission. This is evidenced by comparing the histograms of the residuals. When comparing the histograms in Figures 11 and 12, we notice a markedly lower dispersion in $L(8)/L(250)$ when plotted as a function of $L(3.6)$ than as a function of $L(\mathrm{H}\alpha) + 0.03L(24)$. This is particularly true in the bright regime, where the dispersion relative to $L(3.6)$ is half of that relative to the SFR tracer. In order to verify that the tighter relation with the 3.6 μm image is not a by-product of the presence of the 3.3 μm PAH emission in the IRAC1 band, we perform the same analysis using the PAH—free IRAC2 band (4.5 μm), recovering the same result. We consider this further support of the better association of the 8 μm emission with the heating by evolved stars.

4. DIFFUSE FRACTIONS

We use the plot of $L(8)/L(24)$ versus $L(24)/L(\mathrm{TIR})$ (Figure 6, left) to attempt to separate bins containing dust mainly heated by the diffuse ISRF from those mainly heated by H II regions. We define the diffuse regions as marked by the boundaries $-1.65 \leqslant \log_{10}(L(24)/L(\mathrm{TIR})) \leqslant -1.1$ (or -1.2) and $0.3 \leqslant \log_{10}(L(8)/L(24)) \leqslant 0.7$. While these choices are somewhat arbitrary, we select the region to be symmetric relative to the mean value of $L(8)/L(24)$ (in log scale) at low $L(24)/L(\mathrm{TIR})$, and to be contained within the $L(24)/L(\mathrm{TIR})$ ratio values that mark a relatively constant (and high) $L(8)/L(24)$ ratio. With this choice, we find the fractions of $L(8)$ and $L(24)$ associated with diffuse emission are 80%–59% and 60%–43%, respectively. The range in the fractions is a result of applying the different limits (-1.1 or -1.2) on the selection of data. While these values are uncertain, we always find that the fraction of diffuse $L(8)$ is 33%–42% higher than the fraction of diffuse $L(24)$ independently of how we select the region of diffuse emission. Xilouris et al. (2012) use a different approach from the one presented here, based purely on morphological arguments(decomposing the total emission in the diffuse cold dust in the disk and the dust associated with star forming regions in the spiral arms); yet, they find a similar trend to ours for the fraction of the diffuse emission at 8 μm to be 29%, higher than the value of 21% at 24 μm that those authors derive. Our and Xilouris et al.'s results are slightly different than those of Verley et al. (2009), who derive comparable fractions, 60% to 80% of diffuse emission at both 8 μm and 24 μm. However, our and these authors' results are not necessarily inconsistent when taking into account the different approach used in that work. If the average among galaxies of the diffuse $L(24)$ is in the range 20%–40% (Calzetti et al. 2007; Kennicutt et al. 2009; Leroy et al. 2012), the average diffuse $L(8)$ is in the range 30%–60%, in rough agreement with the results of Crocker et al. (2013) for NGC 628.

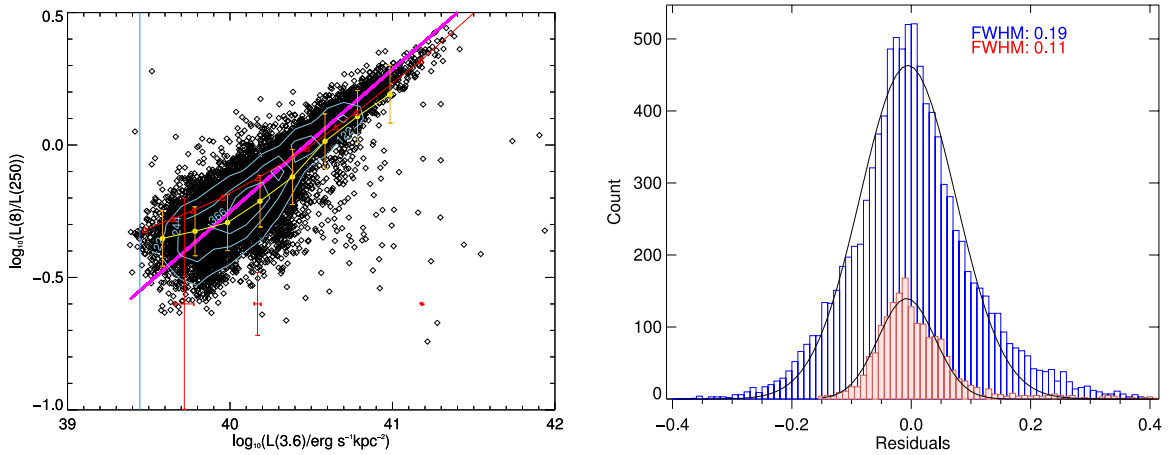

Figure 11. Ratio of $L(8)/L(250)$ vs. 3.6 μm luminosity. Plot symbols and colors are the same as those in Figure 5 for the $q_{\rm PAH} = 0.046$ model. The histogram on the right shows the spread of the data from the best fit line in magenta. The blue histogram is for all the data points to the left, while the red histogram is for data points above $L(3.6) = 3.2 \times 10^{40}$ erg s^{-1} kpc^{-2}.

(A color version of this figure is available in the online journal.)

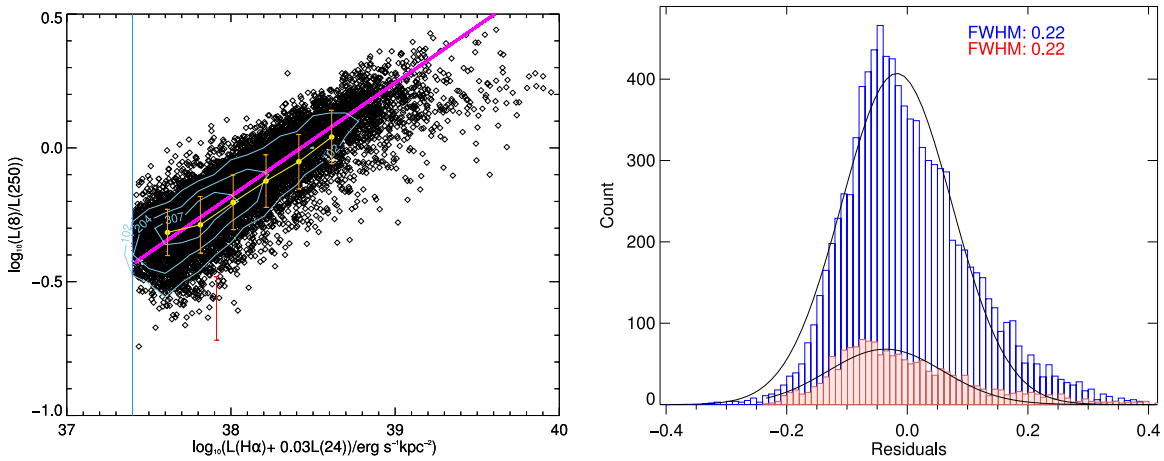

Figure 12. Ratio of $L(8)/L(250)$ vs. a combination Hα and 24 μm luminosity. Plot symbols and colors are the same as those in Figure 5 for the $q_{\rm PAH} = 0.046$ model. The histogram on the right shows the spread of the data from the best fit line in magenta. The blue histogram is for all the data points to the left, while the red histogram is for data points above $L(\mathrm{H}\alpha) + 0.03L(24) = 3.2 \times 10^{38}$ erg s^{-1} kpc^{-2}.

(A color version of this figure is available in the online journal.)

5. CONCLUSION

In this paper, we have investigated the relationships between the 8 μm emission and emission in other wavelengths that are correlated to old stellar populations, star formation, and cold dust. We have also compared our data with the predictions of the models from Draine & Li (2007). Ratios with 24 μm and TIR luminosity show the 8 μm emission to become underluminous in areas of strong 24 μm emission. Taking the 24 μm emission to be the product of heating of dust by young stellar radiation, this implies that 8 μm emission is not a close tracer of young stellar populations, and the carriers responsible for its emission are possibly being destroyed by the intense radiation fields of star forming regions. Furthermore, the behavior of most ($\geqslant$80%) 8 μm emission can be explained using only the $U_{\rm min} = U_{\rm max}$ models, which is valid for diffuse ISRF. We also find that the values of $U_{\rm min}$ that account for the observed 8 μm emission are in the range 0.1–25, consistent with the range found by Draine et al. (2014) for the galaxy M31. When applying a model that includes heating from H II regions, the observed 8 μm values are lower than expected, supporting other authors' conclusions that the carriers responsible for 8 μm emission are destroyed in intense stellar radiation fields. An alternative explanation to the destruction of the 8 μm carriers is to make the PAHs more neutral, suppressing the 8 μm emission and shifting power to the 11–12 μm features(Sandstrom et al. 2012). Mid-IR spectroscopy may discriminate among these two scenarios, although we tentatively give preference to the PAH destruction interpretation.

Ratios of 8 μm with 250 μm emission show a strong correlation with both the TIR and 3.6 μm luminosities. Both 3.6 μm emission and $L(8)/L(250)$ show a similar galactocentric radial trend, suggesting the 8 μm emission may be more connected to old stellar populations than star formation. Further, the $L(8)/L(250)$ as a function of 3.6 μm luminosity shows the tightest relation among those presented in this paper, especially at high luminosity.

We also derive the fraction of 8 μm and 24 μm emission heated either by the ISRF or H II regions. The fraction of $L(24)$ associated with diffuse emission is 60%–43%, while the fraction of $L(8)$ is nearly 33%–42% higher, with 80%–59% of the emission coming from heating by the ISRF.

The results of this study, which support findings by other authors, but at the exquisite spatial resolution enabled by the proximity of M33, suggest that the 8 μm luminosity should not be used as a proxy for measuring and locating star formation in galaxies. Emission in this wavelength is shown in M33 to be more correlated with cold dust or old stellar populations than with star formation.

This work is based on observations made with *Herschel*, a European Space Agency Cornerstone Mission with significant participation by NASA, using the PACS and SPIRE instruments. Partial support for this work was provided by NASA through an award issued by JPL/Caltech.

The *Herschel* spacecraft was designed, built, tested, and launched under a contract to ESA managed by the *Herschel*/Planck Project team by an industrial consortium under the overall responsibility of the prime contractor Thales Alenia Space (Cannes), and including Astrium (Friedrichshafen) responsible for the payload module and for system testing at spacecraft level, Thales Alenia Space (Turin) responsible for the service module, and Astrium (Toulouse) responsible for the telescope, with in excess of a hundred subcontractors.

PACS has been developed by a consortium of institutes led by MPE (Germany) and including UVIE (Austria); KU Leuven, CSL, IMEC (Belgium); CEA, LAM (France); MPIA (Germany); INAF-IFSI/OAA/OAP/OAT, LENS, SISSA (Italy); IAC (Spain). This development has been supported by the funding agencies BMVIT (Austria), ESA-PRODEX (Belgium), CEA/CNES (France), DLR (Germany), ASI/INAF (Italy), and CICYT/MCYT (Spain).

SPIRE has been developed by a consortium of institutes led by Cardiff University (UK) and including Univ. Lethbridge (Canada); NAOC (China); CEA, LAM (France); IFSI, Univ. Padua (Italy); IAC (Spain); Stockholm Observatory (Sweden); Imperial College London, RAL, UCL-MSSL, UKATC, Univ. Sussex (UK); and Caltech, JPL, NHSC, Univ. Colorado (USA). This development has been supported by national funding agencies: CSA (Canada); NAOC (China); CEA, CNES, CNRS (France); ASI (Italy); MCINN (Spain); SNSB (Sweden); STFC, UKSA (UK); and NASA (USA).

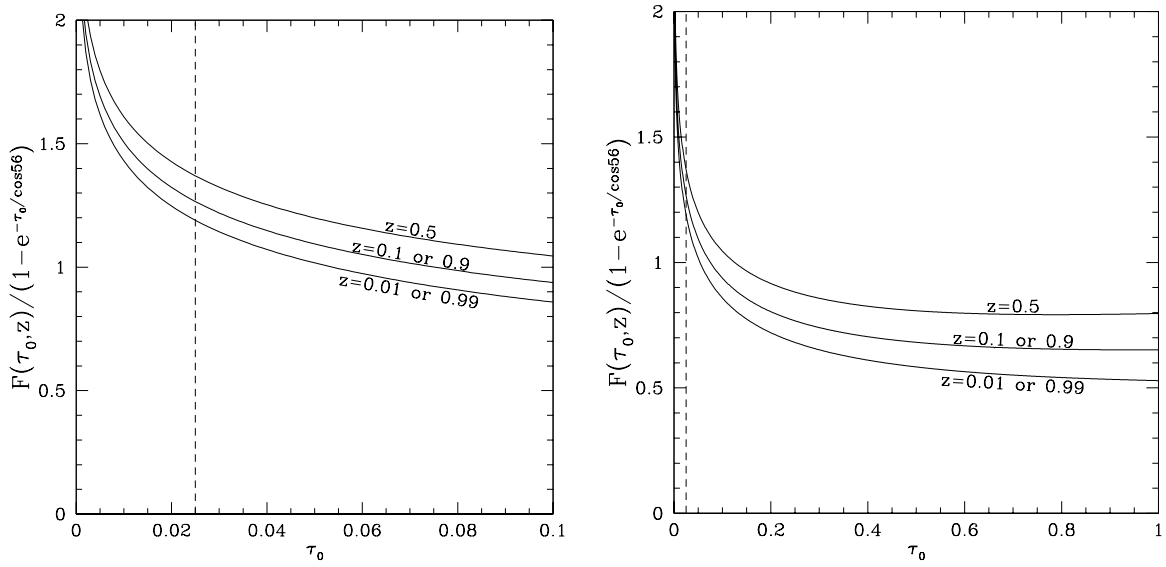

Figure 13. Ratio $F(\tau_0, z)/(1 - e^{-\tau_0/\cos i})$ for the inclination $i \approx 56^\circ$ of M33, as a function of τ_0, the full-thickness optical depth normal to the disk. We see that for $\tau_0 \approx 0.025$ estimated for M33 at 3.6 μm, the ratio $F/(1 - e^{-\tau_0/\cos i}) \approx 1.35$ within the disk. The ratio varies only between 1.4 and 1.2 as we move from the midplane to the surface of the disk.

This research has made use of the NASA/IPAC Extragalactic Database (NED), which is operated by the Jet Propulsion Laboratory, California Institute of Technology, under contract with the National Aeronautics and Space Administration.

APPENDIX

THE RELATION BETWEEN OBSERVED LUMINOSITY DENSITY Σ_ν AND INTERNAL ENERGY DENSITY u_ν

We want to relate the energy density measured within a galaxy to the luminosity surface density measured when viewing a galaxy from the outside, as projected on the sky. This exercise enables us to relate the energy density of ISRF of the MW, which we measure from within the galaxy, to the luminosity density of the ISRF of external galaxies.

For this, we adopt a number of simplifying assumptions, that enable us to perform an analytic calculation.

1. The galaxy is a disk, approximated plane-parallel.
2. The density of stars is everywhere proportional to the density of dust, i.e., the two are homogeneously mixed.
3. The dust is purely absorbing (this assumption is justified if the scattering out of the line of sight roughly compensates the scattering into the line of sight).

Let τ_0 be the dust optical depth normal to the disk. Let $n_\star$ be the density of stars, $L_{\star,\nu}$ the luminosity per unit frequency of one star, n_d be the density of dust, and σ_d be the absorption cross section per dust grain. The equation of radiative transfer is

$$\frac{dI_\nu}{ds} = -n_d \sigma_d I_\nu + \frac{n_\star L_{\star,\nu}}{4\pi} \tag{A1}$$

$$\frac{dI_\nu}{d\tau} = -I_\nu + \frac{n_\star L_{\star,\nu}}{4\pi n_d \sigma_d}, \tag{A2}$$

where $d\tau = n_d \sigma_d ds$.

Because the source function $n_\star L_{\star,\nu}/4\pi n_d \sigma_d$ is constant, this is easily integrated:

$$I_\nu = S_\nu\,[1 - e^{-\tau}], \tag{A3}$$

where τ is the optical depth from the point of interest to ∞, and the source function is

$$S_\nu \equiv \frac{n_\star L_{\star,\nu}}{4\pi n_d \sigma}. \tag{A4}$$

The above equations will now be used to directly relate the energy density measured at some given point within the disk to the disk surface brightness. From any point within the disk, the optical depth normal to the disk is $z\tau_0$ in one direction, and $(1 - z)\tau_0$ in the opposite direction, where $0 < z < 1$. The specific energy density at this point is

$$u_\nu = \frac{1}{c}\int_0^\pi 2\pi \sin\theta d\theta I_\nu(\theta), \tag{A5}$$

where θ is measured relative to the disk normal:

$$u_\nu = \frac{4\pi S_\nu}{c} F(\tau_0, z) \tag{A6}$$

$$F(\tau_0, z) \equiv \int_0^1 d\mu \left[1 - \frac{1}{2}(e^{-z\tau_0/\mu} + e^{-(1-z)\tau_0/\mu})\right]. \tag{A7}$$

Viewed from outside the disk, with inclination i, the intensity is

$$[I_\nu]_i = S_\nu(1 - e^{-\tau_0/\cos i}), \tag{A8}$$

and the apparent specific luminosity surface density (projected on the plane of the sky) is

$$\Sigma_{L,\nu} = 4\pi [I_\nu]_i = 4\pi S_\nu (1 - e^{-\tau_0/\cos i}). \tag{A9}$$

Thus we can relate the energy density within the disk to the disk surface brightness,

$$u_\nu = \frac{4\pi [I_\nu]_i}{c}\frac{F(\tau_0, z)}{1 - e^{-\tau_0/\cos i}} = \frac{\Sigma_{L,\nu}}{c}\frac{F(\tau_0, z)}{1 - e^{-\tau_0/\cos i}}. \tag{A10}$$

We now specialize our derivation to the specific case of M33. Figure 13 shows the ratio $F/(1 - e^{-\tau_0/\cos i})$ as a function of τ_0,

for $z = 0.5$ (midplane), $z = 0.1$ (or 0.9), and $z = 0.01$ (or 0.99), for the estimated inclination $i = 56^\circ$ of M33.

At 3.6 μm, MW dust has $n_d\sigma_d/n_{\rm H} = 2.26 \times 10^{-23}$ cm^2/H. Applying this to the M33 case, with metallicity $\sim$0.5$\times$solar and taking as an example $N_{\rm H} \approx 4 \times 10^{21}$ cm^{-2}, we estimate $\tau_0(3.6\,\mu{\rm m}) = 0.5 \times 2.26 \times 10^{-23} \times 4 \times 10^{21} \times \cos(56^\circ) \approx 0.025$. From Figure 13, we see that $F/(1 - e^{-\tau_0/\cos i}) \approx 1.3$ for this value of τ_0. Thus at 3.6 μm, we estimate $\nu u_\nu \approx 1.3 \times (1/c)\nu\Sigma_{L,\nu}$. For the range of H column densities observed in M33, $N_{\rm H} \sim 4 \times 10^{20} - 6 \times 10^{21}$ cm^{-2}, the range of $F/(1 - e^{-\tau_0/\cos i})$ goes from roughly 1.2 to 1.9, with a corresponding change in the relation between νu_ν and $\nu\Sigma_{L,\nu}$. Taking a mean value $F/(1 - e^{-\tau_0/\cos i}) \sim$1.5 and assuming that the starlight spectrum in M33 is the same as the local ISRF, we get

$$(\nu\Sigma_{L,\nu})_{3.6\,\mu{\rm m}} = \langle U \rangle \times 1.922 \times 10^{40}\ {\rm erg\ s^{-1}\ kpc^{-2}}, \quad \text{(A11)}$$

for the local MW ISRF value $(\nu u_\nu)_{3.6\,\mu{\rm m}} \approx 1 \times 10^{-13}$ erg cm^{-3} (see, e.g., Figure 12.1 of Draine 2011), and using $\langle U \rangle$ for scaling the radiation intensity. We finally include an additional scaling factor f to account for the variations in the gas column density ($f \sim [0.75; 1.25]$):

$$L(3.6) = (\nu\Sigma_{L,\nu})_{3.6\,\mu{\rm m}} = \langle U \rangle \times f \times 1.922 \times 10^{40}\ {\rm erg\ s^{-1}\ kpc^{-2}}, \quad \text{(A12)}$$

as used in this work.

The above treatment assumes the dust and stars to both be smooth plane-parallel distributions, with dust density strictly following stellar density. In a real star-forming galaxy, star-forming regions will have enhanced values of stellar density/dust density, and the stars will also be clumped. Hence, Equation (A12) should be regarded as only a rough estimate for the starlight intensity heating the dust in that pixel.

REFERENCES

Alonso-Herrero, A., Rieke, G. H., Rieke, M. J., et al. 2006, ApJ, 650, 835
Aniano, G., Draine, B. T., Gordon, K. D., & Sandstrom, K. 2011, PASP, 123, 1218
Bendo, G. J., Boselli, A., Dariush, A., et al. 2012, MNRAS, 419, 1833
Bendo, G. J., Dale, D. A., Draine, B. T., et al. 2006, ApJ, 652, 283
Bendo, G. J., Draine, B. T., Engelbracht, C. W., et al. 2008, MNRAS, 389, 629
Bendo, G. J., Wilson, C. D., Pohlen, M., et al. 2010, A&A, 518, L65
Boquien, M., Bendo, G., Calzetti, D., et al. 2010, ApJ, 713, 626
Boquien, M., Calzetti, D., Combes, F., et al. 2011, AJ, 142, 111
Boselli, A., Lequeux, J., & Gavazzi, G. 2004, A&A, 428, 409
Boulesteix, J., Courtes, G., Laval, A., Monnet, G., & Petit, H. 1974, A&A, 37, 33
Braine, J., Gratier, P., Kramer, C., et al. 2010, A&A, 518, L69
Bresolin, F. 2011, ApJ, 730, 129
Calzetti, D. 2012, in Proc. XXIII Canary Islands Winter School of Astrophysics, ed. J. Falcon-Barroso & J. H. Knapen (Cambridge: Cambridge Univ. Press), 419
Calzetti, D., Kennicutt, R. C., Engelbracht, C. W., et al. 2007, ApJ, 666, 870
Calzetti, D., Kennicutt, R. C., Jr., Bianchi, L., et al. 2005, ApJ, 633, 871
Calzetti, D., Wu, S.-Y., Hong, S., et al. 2010, ApJ, 714, 1256
Crocker, A. F., Calzetti, D., Thilker, D. A., et al. 2013, ApJ, 762, 79
Daddi, E., Dickinson, M., Chary, R., et al. 2005, ApJL, 631, L13
Dale, D. A., & Helou, G. 2002, ApJ, 576, 159
Draine, B. T. 2011, Physics of the Interstellar and Intergalactic Medium (Princeton, NJ: Princeton Univ. Press)
Draine, B. T., Aniano, G., Krause, O., et al. 2014, ApJ, 780, 172
Draine, B. T., Dale, D. A., Bendo, G., et al. 2007, ApJ, 663, 866
Draine, B. T., & Li, A. 2007, ApJ, 657, 810
Engelbracht, C. W., Gordon, K. D., Rieke, G. H., et al. 2005, ApJL, 628, L29
Engelbracht, C. W., Rieke, G. H., Gordon, K. D., et al. 2008, ApJ, 685, 678
Fazio, G. G., Hora, J. L., Allen, L. E., et al. 2004, ApJS, 154, 10
Förster Schreiber, N. M., Roussel, H., Sauvage, M., & Charmandaris, V. 2004, A&A, 419, 50
Freedman, W. L., Wilson, C. D., & Madore, B. F. 1991, ApJ, 372, 455
Gordon, K. D., Engelbracht, C. W., Rieke, G. H., et al. 2008, ApJ, 682, 336
Gratier, P., Braine, J., Rodriguez-Fernandez, N. J., et al. 2010, A&A, 522, A3
Griffin, M. J., Abergel, A., Abreu, A., et al. 2010, A&A, 518, L3
Haas, M., Klaas, U., & Binachi, S. 2002, A&A, 385, L23
Helou, G., Roussel, H., Appleton, P., et al. 2004, ApJS, 154, 253
Hinz, J. L., Rieke, G. H., Gordon, K. D., et al. 2004, ApJS, 154, 259
Hodge, P. W., Balsley, J., Wyder, T. K., & Skelton, B. P. 1999, PASP, 111, 685
Hoopes, C., & Walterbos, R. 2000, ApJ, 541, 597
Hunt, L., Bianchi, S., & Maiolino, R. 2005, A&A, 434, 849
Kennicutt, R. C. 1998, ARA&A, 36, 189
Kennicutt, R. C., Jr., Armus, L., Bendo, G., et al. 2003, PASP, 115, 928
Kennicutt, R. C., Jr., & Evans, N. J. 2012, ARA&A, 50, 531
Kennicutt, R. C., Jr., Hao, C., Calzetti, D., et al. 2009, ApJ, 703, 1672
Kramer, C., Buchbender, C., Xilouris, E. M., et al. 2010, A&A, 518, L67
Leitherer, C., Schaerer, D., Goldader, J. D., et al. 1999, ApJS, 123, 3
Leroy, A. K., Bigiel, F., de Block, W. J. G., et al. 2012, AJ, 114, 3
Li, Y., Calzetti, D., Kennicutt, R. C., et al. 2013, ApJ, 725, 677
Li, Y., Crocker, A. F., Calzetti, D., et al. 2010, ApJ, 768, 180
Madden, S. C., Galliano, F., Jones, A. P., & Sauvage, M. 2006, A&A, 446, 877
Magrini, L., Stanghellini, L., & Villaver, E. 2009, ApJ, 696, 729
Mathis, J. S., Mezger, P. G., & Panagia, N. 1983, A&A, 128, 212
McQuinn, K. B. W., Woodward, C. E., Willner, S. P., et al. 2007, ApJ, 664, 850
Meidt, S. E., Schinnerer, E., Knapen, J. H., et al. 2012, ApJ, 744, 17
Pilbratt, G. L., Riedinger, J. R., Passvogel, T., et al. 2010, A&A, 518, L1
Poglitsch, A., Waelkens, C., Geis, N., et al. 2010, A&A, 518, L2
Povich, A., Stone, J. M., Churchwell, E., et al. 2007, ApJ, 660, 346
Reddy, N. A., Dickinson, M., Elbaz, D., et al. 2012, ApJ, 744, 154
Reddy, N. A., Erb, D. K., Pettini, M., Steidel, C. C., & Shapley, A. E. 2010, ApJ, 712, 1070
Regan, M. W., & Vogel, S. N. 1994, ApJ, 434, 536
Relaño, M., Verley, S., Pérez, I., et al. 2013, A&A, 552, A140
Rieke, G. H., Young, E. T., Engelbracht, C. W., et al. 2004, ApJS, 154, 25
Rosolowsky, E., & Simon, J. D. 2008, ApJ, 675, 1213
Roussel, H., Sauvage, M., Vigroux, L., & Bosma, A. 2001, A&A, 372, 427
Sandstrom, K. M., Bolatto, A. D., Bot, C., et al. 2012, ApJ, 744, 20
Smith, J. D. T., Draine, B. T., Dale, D. A., et al. 2007, ApJ, 656, 770
Verley, S., Corbelli, E., Giovanardi, C., & Hunt, L. K. 2009, A&A, 493, 453
Verley, S., Corbelli, E., Giovanardi, C., & Hunt, L. K. 2010, A&A, 510, A26
Verley, S., Hunt, L. K., Corbelli, E., & Giovanardi, C. 2007, A&A, 476, 1161
Werner, M. W., Roellig, T. L., Low, F. J., et al. 2004, ApJS, 154, 1
Xilouris, E. M., Tabatabei, F. S., Boquien, M., et al. 2012, A&A, 543, A74